CHALMERS
UNIVERSITY OF TECHNOLOGY

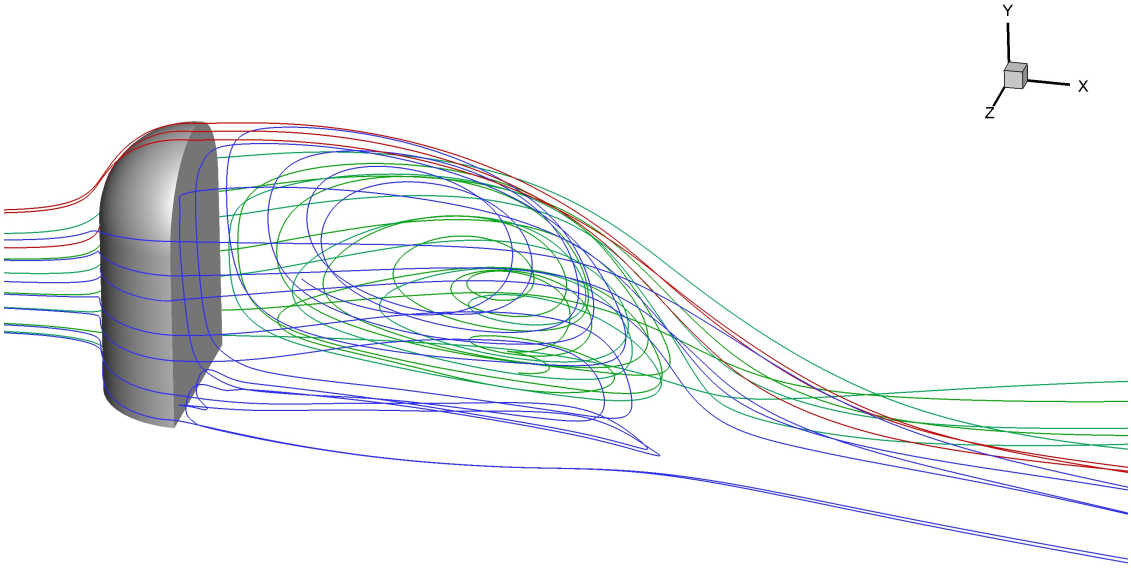

CFD Investigation of a Generic Vehicle Side-View Mirror

Project in Applied Mechanics

Cristóbal Ibáñez
Richard Palm
Ramin Rahani
Xinyuan Shao

Department of Mechanics and Maritime Sciences
CHALMERS UNIVERSITY OF TECHNOLOGY
Gothenburg, Sweden 2020

CFD Investigation of a Generic Vehicle Side-View Mirror
Department of Mechanics and Maritime Sciences
Chalmers University of Technology

Abstract

Electric automobiles are becoming more common in today's society. Since interior car noise can have negative mental health effects for the driver and passengers, it becomes relevant to find out how it is being generated. One important source of noise is the surface pressure fluctuations caused by shear layer impingement and turbulence from the flow around a side-view mirror. Even though many studies about the flow past a side-view mirror have been done, there is not sufficient research for lower speed cases at which electric cars drive at. The purpose of this project is therefore to study the flow around a generic side-view mirror and investigate how it generates noise for some of these cases. The computational fluid dynamics (CFD) software STAR-CCM+, running both steady and unsteady Reynolds-Averaged Navier Stokes (RANS) simulation models is used. Three cases at different freestream speeds of 20, 30 and 40 m/s are simulated. To ensure accurate results, a mesh independence study is carried out for the 40 m/s case with steady RANS simulation. The final mesh is then used to simulate the 20 and 30 m/s cases as well. The steady flow fields were obtained using the realizable $k-\varepsilon$ model and later used as initialization fields for the unsteady cases, were SST $k-\omega$ model is used. Pressure fluctuations data series of specific sensors placed on the surfaces of the mirror and window where analyzed for their power spectral density (PSD) in the frequency domain. For sensors placed in the back of the mirror and on the window inside the recirculation region, noticeable peaks at 500-1300 Hz in the signal's power were observed. Comparison of the PSD's against the Strouhal number revealed that the power peaks are due to coherent structures in the free shear layer developed from the mirror edges. Those PSD peaks will generate tonal noise which is of 500-1300 Hz. Measures should be taken to prevent drivers and passengers from hearing this kind of noise. The present study is also a fundamental step to provide hydrodynamic pressure fluctuation data for a future acoustic wave simulations.

Keywords: side-view mirror, URANS, pressure fluctuation, PSD, SST $k-\omega$ model, realizable $k-\varepsilon$ model.

Contents

List of Figures

List of Tables

1 Introduction

The behaviour of various hydrodynamic properties of the air flow around a generic automobile side-view mirror and its effects on the adjacent surfaces are studied in this project. The computational fluid dynamics (CFD) software STAR-CCM+ is used to carry out the study, and is later compared with existing experimental data from literature. The CFD simulations are carried out using a computer cluster provided by the Swedish National Infrastructure for Computing (SNIC). To accomplish the study 5000 CPU hours per month were granted.

1.1 Background

Side-view mirrors provide better vision for automobile drivers and increase driving safety. Nonetheless, they present one distinct disadvantage, that is, their appearance breaks the integrity of a streamlined shape and induces separation and turbulent flow downstream. The hydrodynamic pressure fluctuations caused by shear layer impingement and turbulence can bring significant noise which could affect the health of the drivers and passengers. As nowadays the car industry pays more attention to the experience of drivers and passengers, reducing the sound level inside the car becomes a big challenge. To achieve this goal, firstly, the magnitudes and distribution of the hydrodynamic pressure fluctuations around side-view mirrors should be studied.

Many studies about side-view mirror have been carried out in recent years. However, most of them are mainly focused on gasoline cars or high speed trains which have higher speed than electric cars. As electric vehicles become more and more popular, it is urgent to estimate the noise generated by side view mirror under lower velocity.

The present study is solely performed using the commercial CFD software STAR-CCM+. Experimental data is taken from past projects that resemble the present CFD simulation conditions to validate the obtained results.

1.2 Project goal

The project goal is to examine and analyze how hydrodynamic pressure fluctuations are generated by a generic side-view mirror model on the downstream side of a car window and to what extent they depend on the velocity. Pressure coefficient, velocity and drag are of particular interest when investigating the hydrodynamic properties and the flow characteristics.

2 Theory

2.1 Drag

Drag is a force that depends on the resistance of motion that flowing fluid causes on an object. The drag coefficient is the dimensionless quantity commonly used to specify the drag quantity of a body and is computed as:

$$C_D = \frac{F_d}{\frac{1}{2}\rho U_\infty^2 A} \tag{1}$$

where F_d is the drag force, ρ is the fluid density, U_∞ is the free-stream velocity and A is the cross sectional area of the side-view mirror.

2.2 Pressure coefficient

The pressure coefficient C_p is the dimensionless quantity that characterizes the relative pressures in the flow field and is defined as:

$$C_p = \frac{p - p_\infty}{\frac{1}{2}\rho_\infty U_\infty^2} = \frac{p - p_\infty}{p_0 - p_\infty} \tag{2}$$

where p is the static pressure at the evaluated point, p_∞ the static pressure in the freestream, p_0 the stagnation pressure, ρ the fluid density and U_∞ the freestream velocity.

2.3 Reynolds number

The Reynolds number (Re) is common used dimensionless quantity to characterize different flow patterns. It is calculated as the ratio between inertial and viscous forces as:

$$Re = \frac{\rho u D}{\mu} = \frac{uD}{\nu} \tag{3}$$

Where ρ is the density, u is the speed of the flow, D is the characteristic length of the interested object in the flow field, in this case, the diameter of the side mirror, and μ and ν are the dynamic viscosity and kinematic viscosity of the fluid respectively.

In this project, for example, one of the cases has a freestream velocity of 40 m/s. The characteristic length of the mirror is $D_{mr} = 0.2$ m, μ is $1.85508{\cdot}10^{-5}$ kg/(m·s) and the density is 1.18415 kg/m^3. Thus the Reynolds number of this case is $Re = 510662.6$.

2.4 Reynolds-Averaged Navier-Stokes Turbulence Models

The Navier-Stokes equations describe the motion of viscous flow. When the flow is turbulent, the instantaneous variables are decomposed into mean and fluctuating components:

$$\phi = \overline{\phi} + \phi' \tag{4}$$

Substituting those decomposed variables into the original Navier-Stokes equation, an additional term $-\rho\overline{v_i'v_j'}$ appears in the momentum transport equation which is the Reynolds stress. One way to model Reynolds stress is using the Boussinesq assumption, which is:

$$-\overline{v_i'v_j'} = \nu_t \left(\frac{\partial \bar{v}_i}{\partial x_j} + \frac{\partial \bar{v}_j}{\partial x_i} \right) \tag{5}$$

Under the Boussinesq assumption, the Reynolds stress is replaced by a turbulent viscosity ν_t. Many turbulent models have been introduced to solve ν_t, for example, $k-\varepsilon$ model and $k-\omega$ model.

2.5 Realizable $k-\varepsilon$ two layers model

In this project the realizable $k-\varepsilon$ two-layer model is used. This model is a combination of the realizable $k-\varepsilon$ model and the two-layer approach. In the realizable $k-\varepsilon$ model a new transport equation for ε is added. Unlike the standard $k-\varepsilon$ model, where the critical coefficient C_μ is constant, here it is expressed as a function of mean flow and turbulence properties. From this, the model can comply certain constraints on the normal stresses consistent with the physics of turbulence. Two-layer refers to that independent of the wall y^+ the model has the ability to either resolve or model the boundary layer. The turbulent eddy viscosity ν_t for the realizable $k-\varepsilon$ two-layer model is calculated as:

$$\nu_t = C_\mu f_\mu k T_e \tag{6}$$

where $C_\mu = 0.09$. f_μ is the damping function that enforces realizability.

The transport equations for the kinetic energy k and the turbulent dissipation rate ε are:

$$\frac{\partial k}{\partial t} + \nabla \cdot (k\bar{v}) = \nabla \cdot \left[\left(\nu + \frac{\nu_t}{\sigma_k} \right) \nabla k \right] + P_k - \varepsilon + S_k \tag{7}$$

$$\frac{\partial \varepsilon}{\partial t} + \nabla \cdot (\varepsilon\bar{v}) = \nabla \cdot \left[\left(\nu + \frac{\nu_t}{\sigma_\varepsilon} \right) \nabla \varepsilon \right] + \frac{\varepsilon}{k\rho} c_{\varepsilon 1} P_\varepsilon + c_{\varepsilon 2} f_1 \frac{\varepsilon^2}{k} \tag{8}$$

For brevity, here all details of this model wont be covered, but more information on the constants values and so on, can be found on Wilcox's book [1].

2.6 SST $k-\omega$ model

The $k-\omega$ model is a model that solves transport equations for the turbulent kinetic energy k and the specific dissipation rate ω to determine the turbulent viscosity ν_t. The $k-\omega$ model has enhanced performance for boundary layers under unfavorable pressure gradients, compared to the $k-\varepsilon$ model [1]. By substituting variables, the ε transport equation from the standard $k-\varepsilon$ model can be transformed into an ω transport equation. A blending function is used to mix the use of both models. The

$k-\varepsilon$ model is implemented in the far-field and the $k-\omega$ model near the wall. The turbulent eddy viscosity ν_t is calculated as:

$$\nu_t = kT \tag{9}$$

where T is the turbulent time scale. It is calculated using Durbin's realizability constraint:

$$T = min\left(\frac{\alpha^*}{\omega}, \frac{a_1}{SF_2}\right) \tag{10}$$

The transport equations for the kinetic energy k and the specific dissipation rate ω:

$$\frac{\partial k}{\partial t} + \nabla \cdot (k\bar{v}) = \nabla \cdot \left[(\nu + \sigma_k \nu_t)\, \nabla k\right] + P_k - \beta^* \rho \omega k \tag{11}$$

$$\frac{\partial \omega}{\partial t} + \nabla \cdot (\omega \bar{v}) = \nabla \cdot \left[(\nu + \sigma_\omega \nu_t)\, \nabla \omega\right] + P_\omega - \beta \omega^2 + 2\,(1 - F_1)\, \frac{\sigma_{\omega 2}}{\omega} \nabla k \cdot \nabla \omega \tag{12}$$

For more details of SST $k-\omega$ model, one can check Menter's paper [2].

2.7 Wall y^+

The non-dimensional quantity for the wall distance y is defined as:

$$y^+ = \frac{y \rho u_*}{\mu} \tag{13}$$

where μ is the dynamic viscosity, ρ the density, and u_* the friction velocity. This last variable is a form by which the shear stress may be re-written in velocity units:

$$u_* = \sqrt{\frac{\tau_w}{\rho}} \tag{14}$$

where the wall shear stress τ_w can be expressed as:

$$\tau_w = \mu \frac{du}{dy}\bigg|_{y=0} \tag{15}$$

If a desired y^+ wants to be achieved close to the wall, then the height y of the first cell needed for this can be obtained from Eq.(13). Since the friction velocity u_* is unknown before running the simulation, an educated guess of $u_* = 0.05 U_\infty$, where U_∞ is the free-stream velocity, can be used. After simulating the flow field, changes to the first height cell can be made considering the actual results obtained for the wall y^+.

2.8 CFL number

CFL number is related to the convergence while solving the Navier-Stokes equations. In one-dimensional case, it is calculated as:

$$CFL = \frac{u \Delta t}{\Delta x} \tag{16}$$

It is relevant to the local speed, time step and mesh size. CFL number of every cells should be kept at a relative value to maintain the stability of the simulation.

3 Methodology

3.1 Geometry

The generic side-view mirror is modeled using CATIA V5, based on the geometries stated in Yao and Davidson [3]. The mirror has a total height of 0.3 m and is formed as a half cylinder with a rounded end shape as Figure 1 shows. The radius of both the half cylinder and the spherical end is 0.1 m. The mirror is attached on a surface which represents a rigid plate. Within the rigid plate a surface which represents a window is defined. Both plate and window use the same wall boundary and they are in different patches just for the convenience of data extraction. The computational domain is a 8.1m × 2.3m × 4m cuboid as shown in Figure 2.

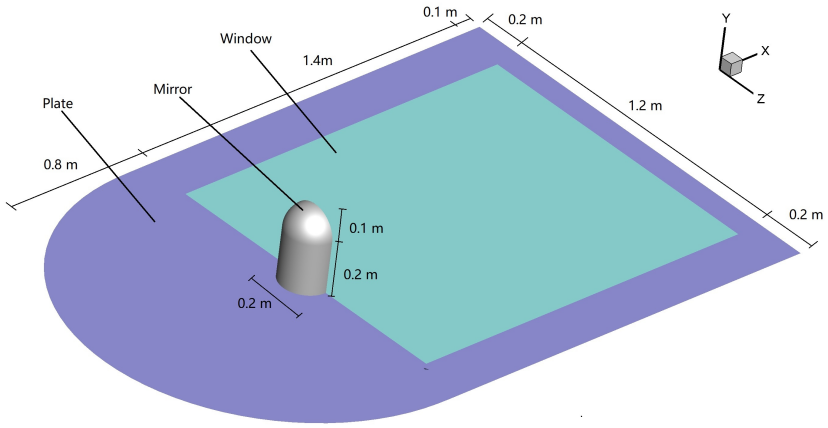

Figure 1: Geometry of the mirror attached to the rigid plate.

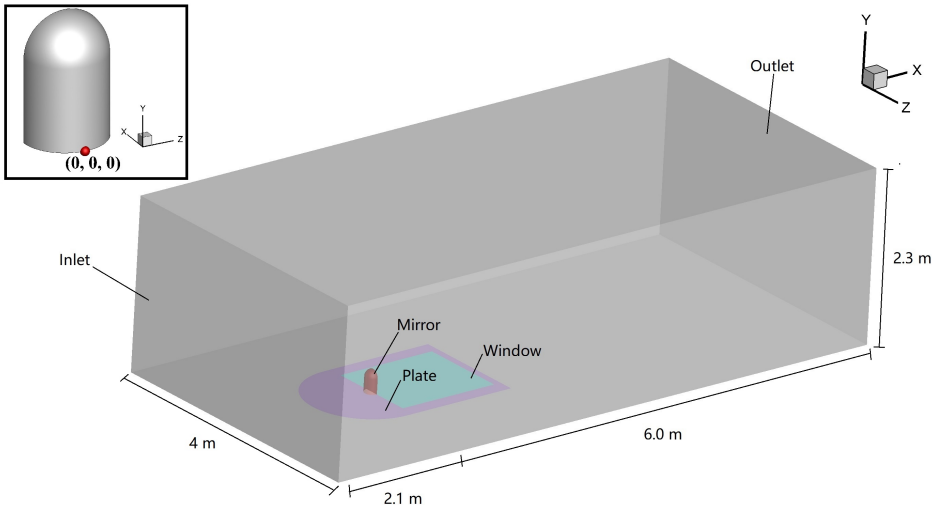

Figure 2: Computational domain and placement of the mirror, where the origin of the coordinate system is noticed as a red dot.

3.2 CFD simulations

The CAD model of the side-view mirror and plate, together with the cuboid, are imported from CATIA V5 to STAR-CCM+ for the simulations. All simulation cases are listed in Table 1. It is to be noticed that flow passage time is the time the flow takes to go through the computational domain at its freestream velocity.

Table 1: Simulation cases

Cases number	Inflow speed	Re	Flow passage time	Simulation type
Case 1	20 m/s	2.55×10^5	0.4 s	RANS
Case 2	30 m/s	3.83×10^5	0.27s	RANS
Case 3	40 m/s	5.11×10^5	0.2 s	RANS
Case 4	20 m/s	2.55×10^5	0.4 s	URANS
Case 5	30 m/s	3.83×10^5	0.27 s	URANS
Case 6	40 m/s	5.11×10^5	0.2 s	URANS

3.2.1 Fluid properties

In this project, the fluid of interest is air. Its properties are set to dynamic viscosity $\mu = 1.85508 \cdot 10^{-5}$ kg/(m·s) and density $\rho = 1.18415$ kg/m^3.

3.2.2 Boundary conditions

The mirror, the plate and the window were all set as wall boundaries. Symmetry boundary condition is set to the sides of the cuboid, except the inlet and the outlet (see Figure 2). The inlet is instead set with a velocity inlet boundary condition, and the outlet with a pressure outlet boundary condition. The inlet velocity is initially given as 40 m/s, which is used for the mesh independence study. Afterwards, the inlet velocity is adjusted according to other cases, which are 20 m/s and 30 m/s. The outlet is defined as a pressure outlet with gauge pressure equal to 0 Pa. This means that at the outlet the pressure is the atmospheric pressure $p_\infty = 101325$ Pa.

3.2.3 Mesh generation

The mesh is generated using the automated mesh operation built inside STAR-CCM+. Since the computational domain is three dimensional, a volume mesh is created. This volume mesh consists of polyhedral cells, which occupy most of the computational domain, except close to the wall surfaces. These instead consist of prism layer cells. The prism layer cells are orthogonal prismatic cells near to wall surfaces or boundaries which can improve the accuracy of the simulations. Several sections of the mesh can be seen in Figure 4.

Several settings in STAR-CCM+ are used to control how many mesh cells that should be created and which size they should have. Regions with more and smaller cells will give finer details and more accurate results, but in return requires more computational effort. This in the end becomes a balancing act between computer

performance and results that are accurate enough. It is also important to specify where more and smaller cells are needed.

A built in function of STAR-CCM+ is wake refinement. This function can control the mesh to become more detailed in a region where a wake is to be expected. In this case, theoretically, a separation should form behind the mirror. That is why wake refinement is applied from the back of the mirror. This wake refinement stretches 1.45 m (7.25 D_{mr}) from the back of the mirror, with a spread angle of 10 degrees.

3.2.4 Mesh independence study

A mesh independence study was performed to assess if the mesh for the simulations gives results that are accurate enough. The goal with this is to find a good detail level of the mesh, to ensure that a finer mesh does not give any significant changes in results, and thus making sure that unnecessary computer power is not being used. Three different meshes, with different settings for cell sizes were made for comparison. Table 2, in the result section, shows the different parameters used for the three meshes called coarse, medium and fine.

3.2.5 Steady RANS simulations

Steady simulations were performed using the realizable $k - \varepsilon$ model firstly for the mesh independence study. Later, the other case velocities were simulated using the same model in steady mode. After, the resulting solution fields were used as initial flow fields for the unsteady simulations.

3.2.6 Unsteady RANS simulations

For the same case velocities, unsteady (URANS) or time varying simulations were run by using the SST $k - \omega$ model. The goal was to measure the time development of the instantaneous variables and their fluctuations, as well as time-averaged quantities from unsteady simulations. These give more accurate results than the averages from steady simulations because more is being resolved and less is being modeled compared to steady RANS.

The URANS simulations were set to run for three flow passages. A flow passage is when a fluid particle in the free stream supposedly has been transported from the inlet to the outlet. Probes measuring velocity and pressure coefficient were positioned on specific locations of the domain such as on the window or mirror surfaces. This instantaneous data was saved and collected throughout the whole span of the time simulated. Additionally time-averaged quantities in every cell of the domain were stored. This time-averaging processes was started after the first flow passage to ensure that the fluctuations are oscillating in a stable manner, so that the mean value is reliable.

4 Results and Discussion

The following section presents the main results of the CFD simulations. First, the mesh features along with the mesh independence study results are discussed. Later, the steady flow solutions for the three case velocities are analyzed, including drag force, velocity, pressure and wall shear stress. At last, instantaneous field, as well as fluctuations and time-averaged quantities are studied and contrasted with experimental data to validate results for the unsteady simulations.

4.1 Mesh independence

The mesh independence study is carried out with a steady state simulation and the $k-\varepsilon$ model. The simulated case is the maximum inlet velocity of 40 m/s. As Eq. (13) indicates, with velocity decreasing, y^+ will also decrease, which means that the mesh made for velocity 40 m/s also fulfill the $y^+ < 1$ requirement under the velocity of 20 m/s and 30 m/s. This study resulted in comparing three meshes with different total number of cells and refinement features. In Table 2 the main different parameters for each mesh has been compiled for comparison.

As shown, the total number of cells ranges from 2.37 million cells to 5.29 million cells. The prism cells are kept with the same total thickness through all three meshes, and the only difference is that for the fine mesh the number of layers are added with one extra from 15 to 16 layers. The prism layer first cell thickness size near the wall was estimated as explained in Section 2.7, where the value of the friction velocity u_* is approximated as $0.05v_\infty$. The main difference between those three meshes is the base size which determines the overall default size of the cells and the parameters of wake refinement, for example, the isotropic cell size and the growth rate of the wake region.

Table 2: Mesh parameters

	Coarse	Medium	Fine
Number of prism layers	15	15	16
Prism layer near wall thickness (10^{-6} m)	9.275	9.275	9.275
Prism layer total thickness (m)	0.005	0.005	0.005
Base size (mm)	8	7	6
Mesh density	1.05	1.1	1.1
Growth factor	0.9	0.9	0.9
Wake refinement - isotropic size (mm)	7	6	5
Wake refinement - growth rate	1.15	1.1	1.1
Wall y+	~ 1	~ 1	~ 1
Total number of cells (10^6)	2.37	3.51	5.29

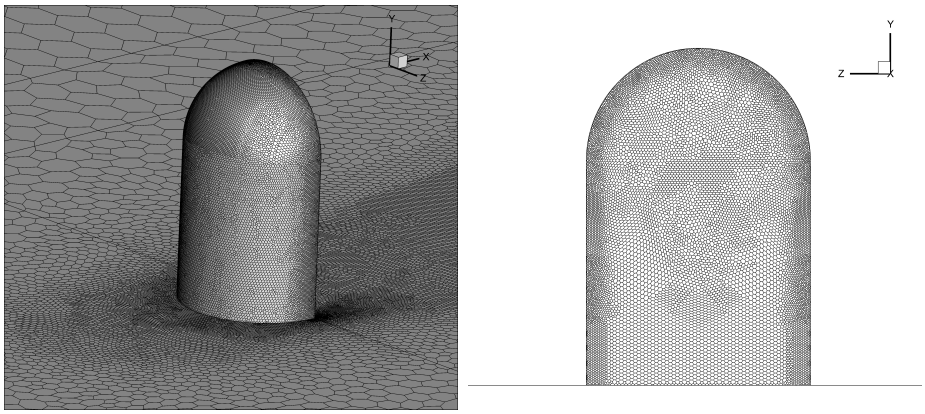

Figure 3: Left: cell distribution of the mirror front surface, right: cell distribution of the mirror back surface.

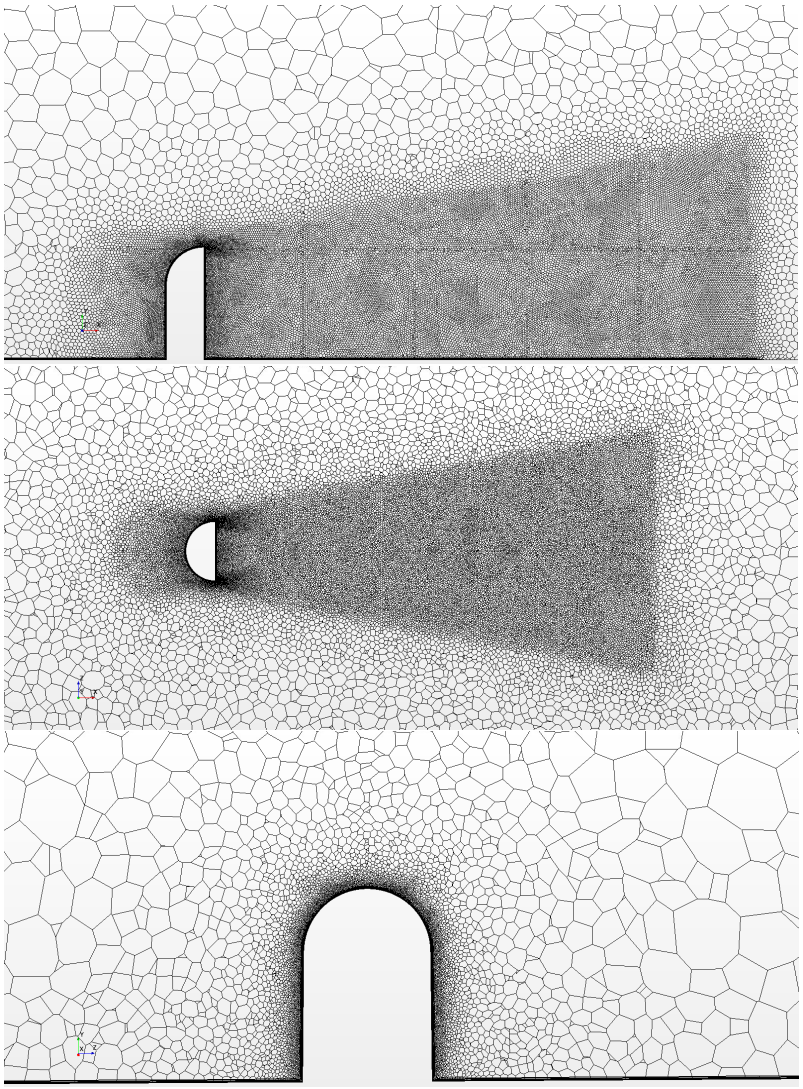

Figure 4: Cut planes of the medium mesh, from top to bottom: xy-plane at $z = 0$ m, xz-plane at $y = 0.1$ m, yz-plane at $x = 0.098$ m

As previously described, three different meshes, coarse, medium and fine were compared. The medium mesh was chosen, in order to save computational time, since the accuracy was only slightly different compared to the fine mesh. Further optimization of the mesh could be done, such as adjusting different regions of the mesh, e.g. the wake region. But since this is a time consuming process and only negligible changes would appear, further investigation was considered to be unnecessary for this case.

Figure 3 shows the mesh resolution for the side-view mirror body for the medium mesh. It is a requirement that the grid over the surface of the body should at least be fine enough to resolve the curved geometry of the object. As seen in Figure 3, the mesh resolution on the body is capable of resolving the semi-sphere and cylindrical shape of the generic side-view mirror. For the sake of brevity only the medium mesh on the mirror is shown in Figure 3. Nevertheless, all three mesh resolutions accomplish the task of resolving the body geometry with much more than 50 cells along each mirror edge (bottom curved, left and right edges).

To better resolve the wake generated behind the blunt body, a wake region with refined features is located downstream the side-view mirror. In Figure 4, several cut planes of the medium mesh are shown where the wake refinement as well as prism layers can be clearly seen.

One of the variables that can be assessed and compared in the mesh independence study is the force along the x-axis exerted on the blunt body by pressure and flow viscosity in the form of the drag coefficient. Table 3 shows the dimensionless drag force coefficients for the different meshes. It is noticed that the difference between them is small enough to be ignored, as the third row suggests, the error of the coarse mesh is only 1.32%. Therefore, the drag force coefficient can be predicted fairly well by even using the coarse mesh.

Table 3: Drag coefficient for three different meshes and the error with respect to the fine mesh.

	Coarse	Medium	Fine
C_d	0.5305	0.5241	0.5236
Error (%)	1.32	0.11	-

Another interesting variable to compare in this case is the pressure coefficient along the side-view mirror surface. Figure 5 shows how the pressure coefficient varies for the three meshes along a line on the front and back surface of the mirror. It can be seen that for the front line, which is facing the incoming flow, the pressure coefficient C_p does not vary considerably for the different meshes. For a part of the front which is located at the bottom cylinder, C_p is close to 1. That is because the flow is stagnated there and the static pressure is exactly equal to the total pressure. On the other hand, the back line along the mirror exhibit more visible differences between different meshes. It is shown that the medium mesh results are closer to the refined solution than the coarse grid.

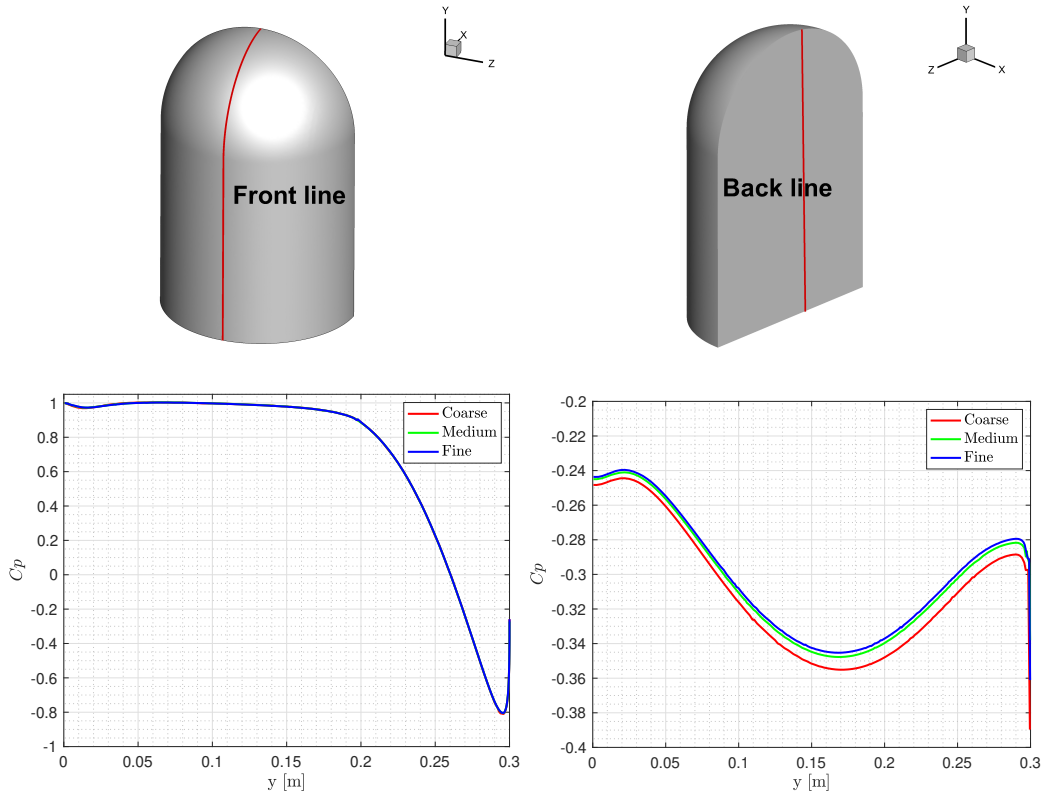

Figure 5: Pressure coefficient distribution along the center line of the mirror front and back, left: front line, right: back line

Figure 6 shows the location of 4 different profile lines placed along the wake region projected on $z = 0$ plane and their correspondents velocity profiles for v_x. These comparisons show that at each location the velocity profiles resemble each other well for the three different meshes. However a detailed inspection shows that the medium mesh velocity profiles resemble the finer results better than the coarse grid profiles, for v_x. The first three profiles closest to the mirror show velocities with negative values as we move close to the window. This shows that recirculation occurs close to the back side of the mirror and that at $x = 1$ m, it does not occur anymore.

All three different grid variations present a similar wall y^+ distribution over the plate and the blunt body. This is because, as previously explained, the prism layer features are not drastically changed so the wall y^+, obtained by the estimated first layer thickness under velocity 40 m/s, does not vary severely. Figure 7 displays the wall y^+ distribution for the 40 m/s case. It is seen that the value of the wall y^+ is kept around one in the majority of the solid boundaries except in the cells near the edge of the plate. This phenomenon is caused by the sudden change in boundary conditions (from symmetry to no-slip wall) which gives a high wall shear stress close to the edges.

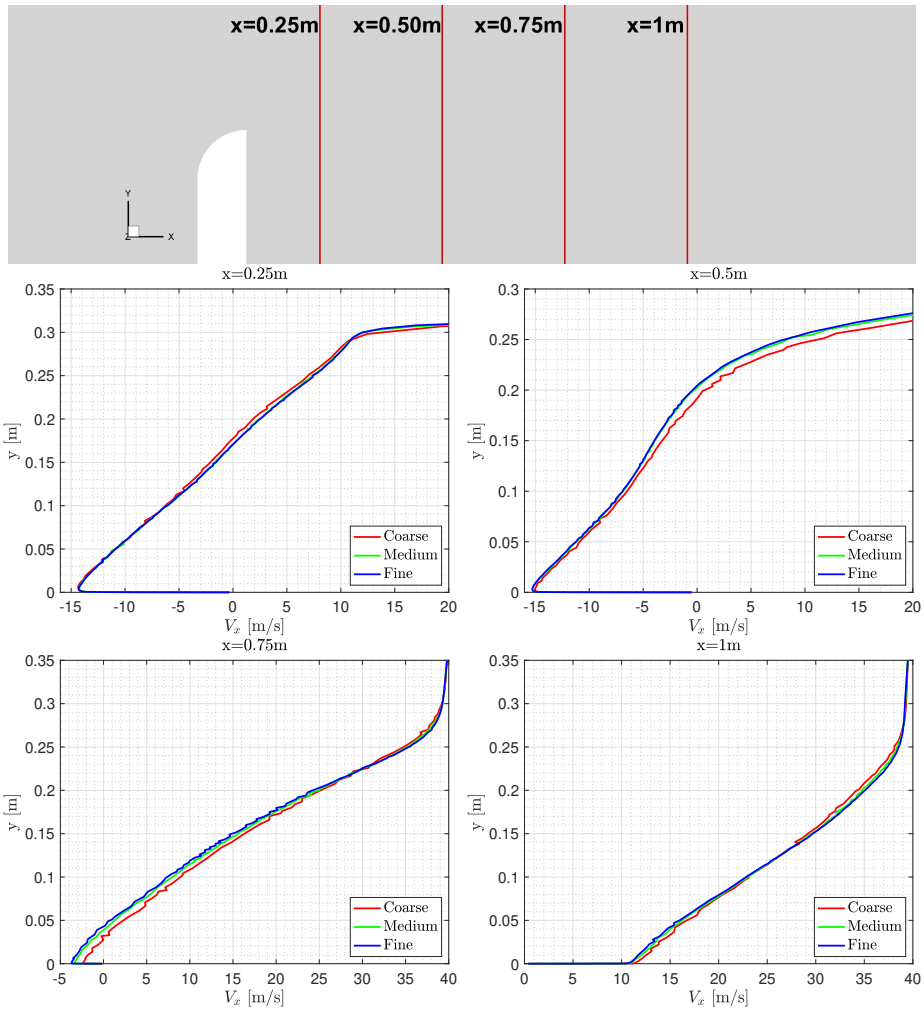

Figure 6: Velocity profiles along different x positions. Top: red lines indicate the location; bottom 4 pictures, from top to bottom, left to right are velocity profiles at $x = 0.25$ m, $x = 0.5$ m, $x = 0.75$ m and $x = 1$ m respectively.

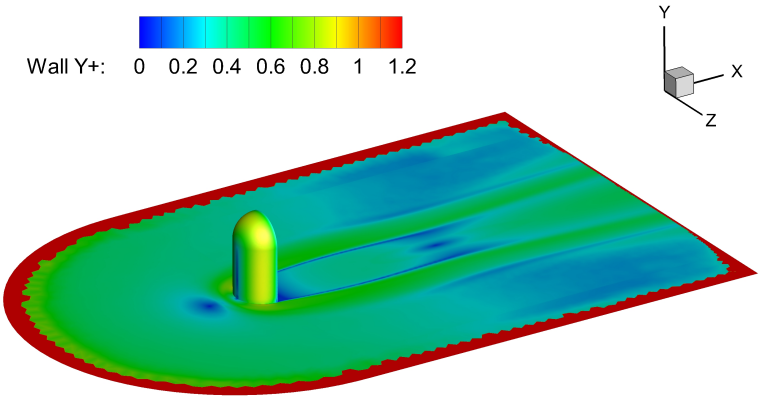

Figure 7: Wall y^+ at $v_x = 40$ m/s for the steady simulation

Since the meshes gave similar results, a finer mesh would only give negligible improvements to the results. Therefore, no other mesh was done for the mesh independence study. The coarse grid showed pressure distribution and velocity profiles that deviates a bit from the fine mesh. However, the medium mesh deviates only slightly in comparison with the finer one, and is therefore considered to be a mesh with adequate accuracy. Once the medium mesh has been selected the rest of the cases with different velocities can be simulated and the results can be expected to be mesh independent as well.

4.2 Steady field

Firstly, steady simulation are carried out to obtain a first understanding of the mean flow field. The results of each steady simulation are also the initial fields of the corresponding unsteady simulations later on.

4.2.1 Drag force

The following table presents the drag force and drag coefficient on the side-view mirror for the three different simulated velocities. As expected, the drag force related to slow velocities is lower than for higher velocities, while the drag coefficient only vary slightly since the shape and the cross section area is kept the same for the side-view mirror. The 20 m/s and 30 m/s cases give drag coefficients that are 2.95 % and 1.15 % larger than the 40 m/s case respectively.

Table 4: Drag force and drag coefficient for three different velocities

Velocity	20 m/s	30 m/s	40 m/s
Drag (N)	7.1194	15.7389	27.6611
C_d	0.5397	0.5303	0.5242

4.2.2 Velocity and pressure distribution

The steady fields for velocity v_x and pressure coefficient for the three different cases are shown in Figure 8. The velocity v_x is normalized by the freestream velocity v_∞. Although the three cases have different freestream velocity, after normalizing, all of them have similar v_x/v_∞ distribution. Generally speaking, the velocity field has a fast region right on top of the blunt body extending downstream above the recirculation region which can be clearly seen in the streamline plot. Inside the recirculation region a "peak-shape" of negative velocities is noticed. Also, there is a small negative velocity region that appears in front of the side-view mirror. This region of the flow seems to re-circulate. This can be verified by looking at the streamlines from the right figure. This phenomenon is known as the horseshoe vortex.

As for the distribution of C_p, the relative contour shows that there is a high pressure region on the front side of the mirror. As the flow passes through the curved surface, it is accelerated and creates a large low pressure area after the back of the mirror.

Similar to the velocity distribution, the fields of C_p also show similarities between cases of different velocities.

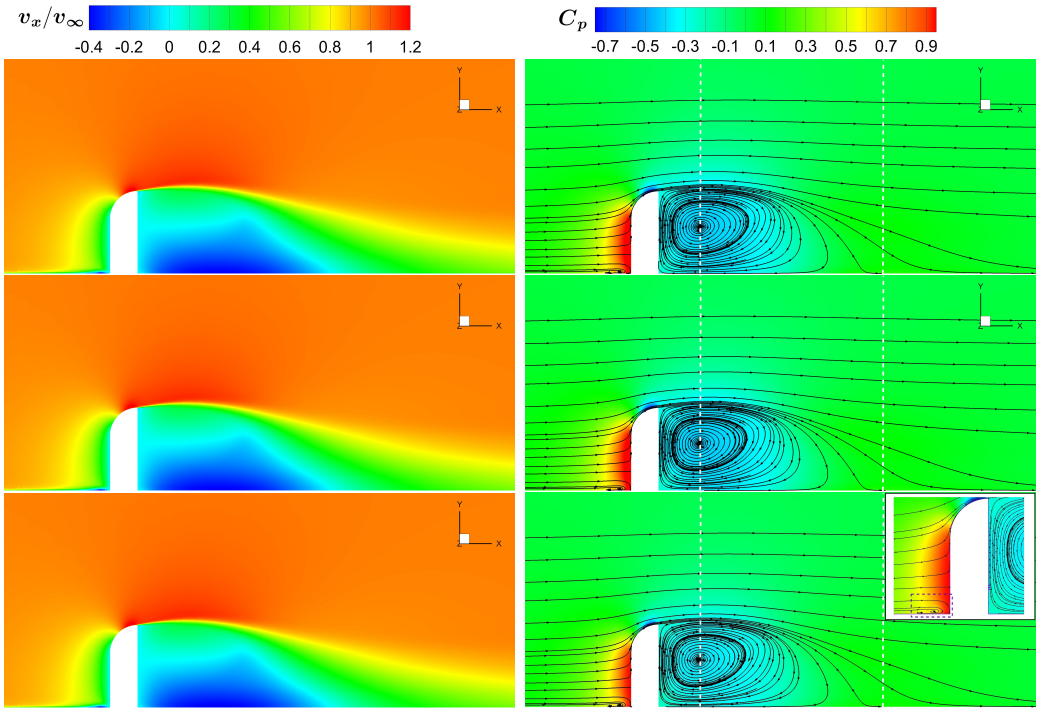

Figure 8: Normalized velocity v_x (left column) and pressure coefficient distribution (right column) cut plane $z = 0$. 20 m/s (top), 30 m/s (middle) and 40 m/s (bottom).

4.2.3 Wall shear stress and recirculation region

To better understand how long the extension of the recirculation region for each velocity is, Figure 9 illustrates wall shear stress on a line located at the surface of the window for the three different steady solutions. The length of the recirculating region is the length span where the wall shear stress is negative after the mirror. This is due to the definition of the wall shear stress in Eq. 15 which is proportional to the gradient of velocity in the normal wall direction ($\partial v_x/\partial y$). Since the wall has a no slip condition ($v_x = 0$ at the wall), the wall shear stress being negative, means that the gradient of velocity in normal wall direction is negative as well. This can only imply that v_x decreases from zero to negative value moving away from the wall.

It is shown, in Figure 9, that for the three different velocities the length of the mean recirculation region is very similar. This result is in accordance to what can be seen in Figure 8, both in the streamlines and the velocity contours. Only a closer look can distinguish that for the slowest velocity, the length of the recirculation region is larger than for the fastest air speed. However the magnitude of the wall shear stress is in accordance with what was previously expected. For bigger velocity, the wall shear stress magnitude is larger.

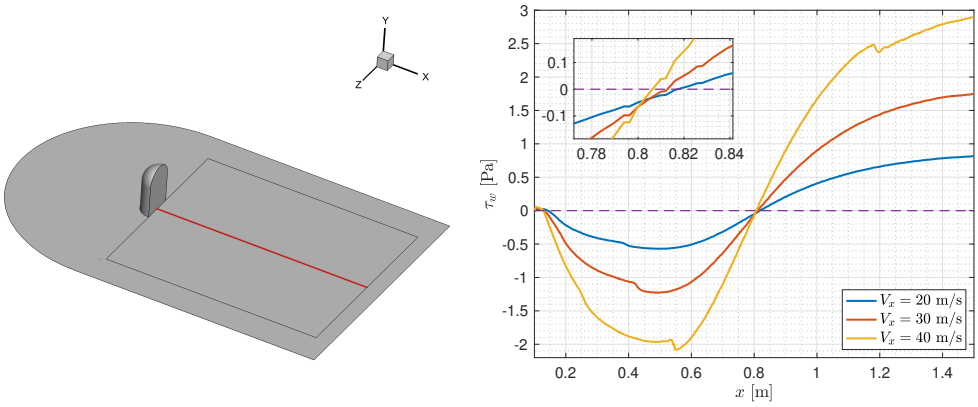

Figure 9: Wall shear stress τ_w in x direction along a line, the left figure shows its position

4.3 Unsteady field

In order to save computational resources, the unsteady cases are initialized with the steady field results. After initialization, three cases are run in unsteady mode for three full flow passages each. By doing this, we ensure that the instantaneous variables are fluctuating in a stable manner around a certain constant mean value.

4.3.1 Turbulence model

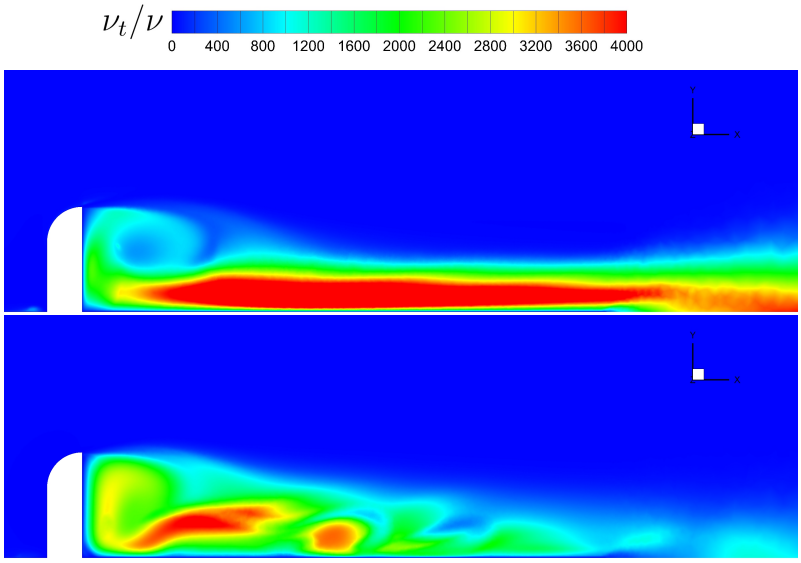

Figure 10: ν_t/ν of the xy cross section ($z = 0$) at $t = 0.39s$ for freestream velocity equals to 40 m/s. Above: $k - \varepsilon$ model. Below: SST $k - \omega$ model.

The realizable $k - \varepsilon$ model is used and works quite well in steady simulations. However, it is not applicable for the unsteady simulations since it cannot provide an unsteady solution starting from the same steady field. In order to find the reason, the ratio ν_t/ν is investigated as shown in Figure 10. In the wake region, the realizable

$k-\varepsilon$ model gives much larger ν_t than SST $k-\omega$ model does, which is one of the reasons why the realizable $k-\varepsilon$ model performs poorly in these unsteady cases. The large ν_t in the wake region dampens the fluctuations and makes the unsteady field look like a steady one. Therefore, the SST $k-\omega$ model is chosen for the unsteady cases.

4.3.2 CFL number

Table 5 summarizes the achieved CFL numbers, the time step sizes and the simulated total times for the three unsteady simulations. The maximum CFL number was limited to a value around 11 to ensure reliability of the results as well as convergence.

After one flow passage all three unsteady simulations presented a stable behaviour. Therefore, the time averaging of field variables, such as velocity in the entire domain, was considered from this point on until the end of the simulation.

Table 5: The parameters of the URANS simulation.

Case	Δt (s)	max CFL	Total time (s)	Flow passages
URANS 40	3×10^{-5}	$\sim$ 12.1	0.6	3
URANS 30	4×10^{-5}	$\sim$ 11.9	0.8	3
URANS 20	6×10^{-5}	$\sim$ 11.4	1.2	3

4.3.3 Flow field characteristics

Figure 11 shows a comparison between the average pressure coefficients $\langle C_p \rangle$ for the steady and unsteady case at 40 m/s with experimental data obtained from Höld et al. [4] and Siegert et al. [5] at different individual sensors placed over the mirror surface. The sensor locations are also shown in Figure 11. The specific coordinates of those sensors can be checked in Table A.1. It can be seen that the unsteady simulation, which uses SST $k-\omega$, presents a $\langle C_p \rangle$ that is closer to the experimental data than its steady counterpart where the realizable $k-\varepsilon$ model is used. Nevertheless, the difference between them is relatively small, especially for sensor 10 to 25 placed in the front of the mirror, where simulations and experimental data are almost exactly matched. That means, if only the time-averaged $\langle C_p \rangle$ is of great interest, steady RANS is a relatively good and economical option.

Figure 12 displays certain streamlines of the time-averaged velocity field. The streamlines from the left and right edge of the mirror make up of the recirculation bubble while the streamlines from the top edge of the mirror impinge directly on the plate. This impingement region introduces large pressure and velocity fluctuations.

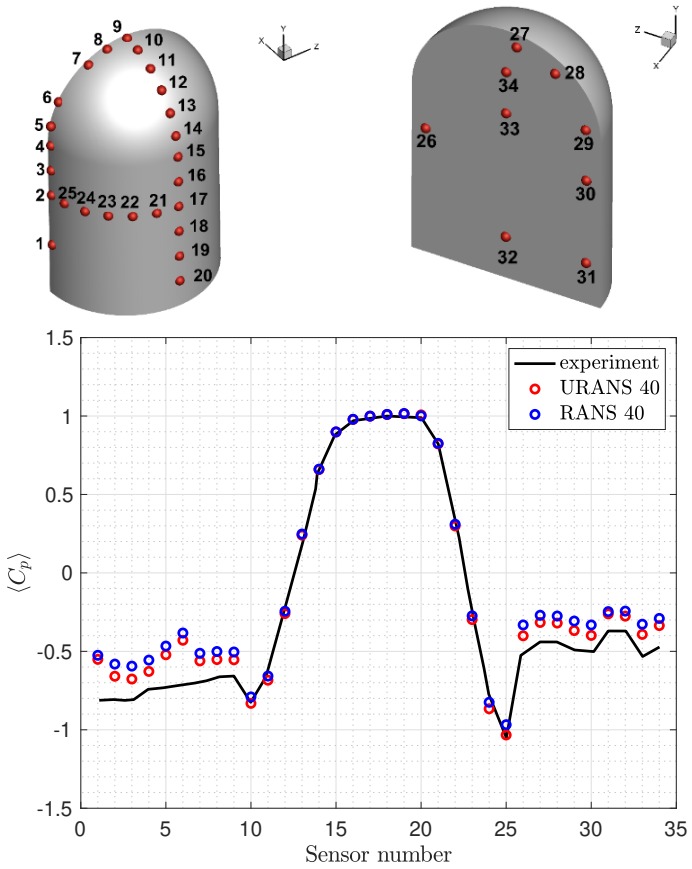

Figure 11: The time-averaged pressure coefficient, v_x=40 m/s

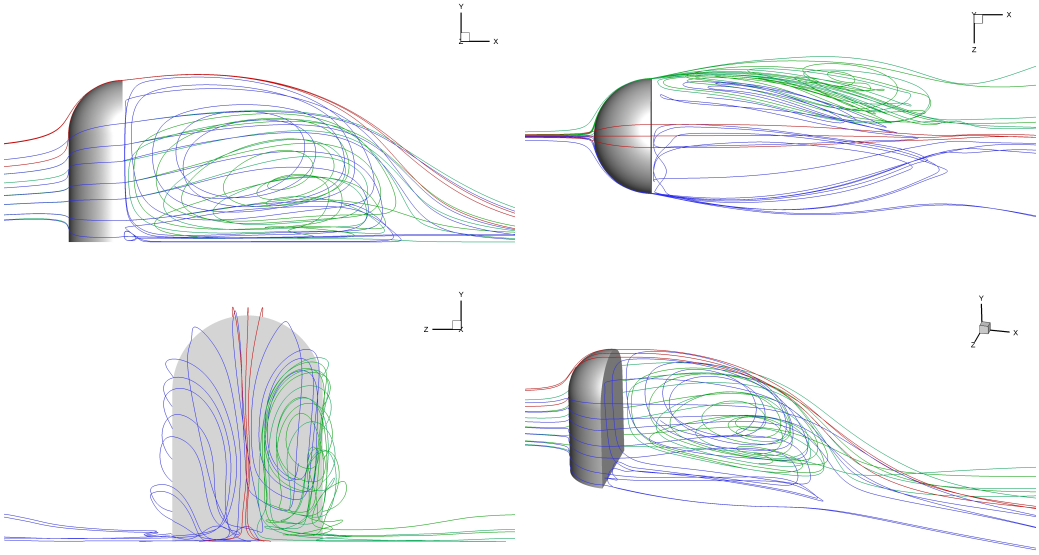

Figure 12: Streamlines of the time-averaged velocity field from different views. Streamlines from the upper edge of the mirror are colored in red and those from the left and right mirror side are colored in blue and green respectively.

It is interesting to check the instantaneous vorticity distribution to have a better picture of the turbulent structures developing downstream the mirror. Figure 13 shows the dimensionless vorticity component $\omega_x D_{mr}/U_\infty$ at one xz cross plane at $y = 0.01$ m and the physical time of this snapshot is 0.39 s. It can be seen that in the dashed box region, the free shear layer originates at the mirror's edge becoming unstable as it goes downstream. This structure has a certain frequency and it causes pressure and velocity fluctuations downstream. From the top figure it is shown how, ultimately, the vortices evolve and merge with the larger weak vortices as they move further downstream.

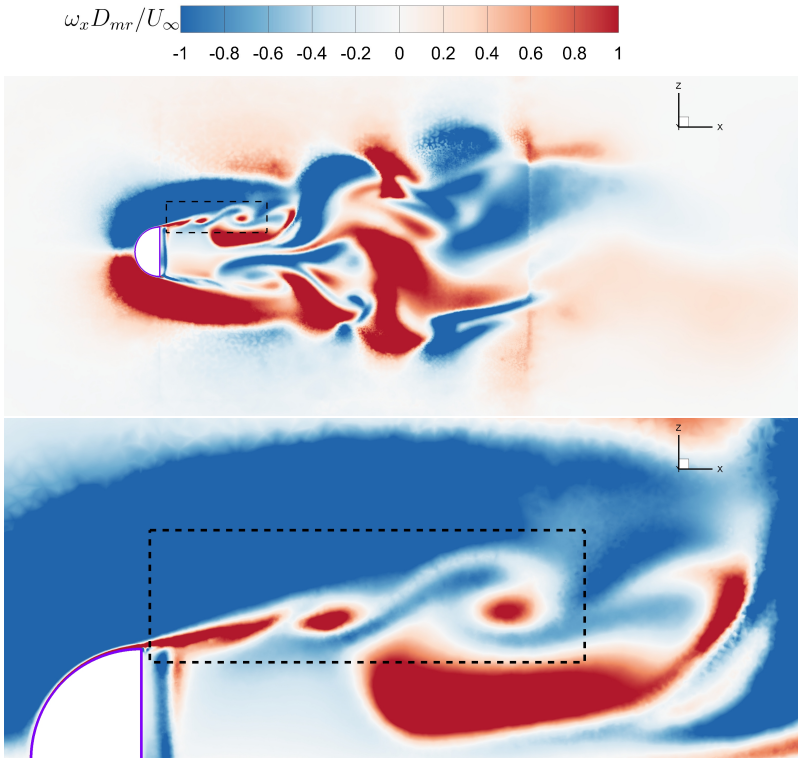

Figure 13: Vorticity at t=0.39s, xz plane at $y = 0.01$ m

4.3.4 Pressure fluctuations

Time domain

Figure 14 gives the pressure fluctuations, $p' = p - \langle p \rangle$, in the time domain at three sensor positions which are H1, H2 and H3. The position of these sensors is shown in Figure 15. H1 is at the back surface of the mirror close to its edge while H2 and H3 are located on the window surface. Specifically, H2 is in the region impinged by the recirculation bubble and H3 is in the region impinged by the shear layer stemmed from the edge of the mirror [6].

Comparing the pressure fluctuation magnitudes of different velocities at the same sensor position, it is clear that the amplitude of the fluctuations is related to the velocity. The higher the velocity, the greater the magnitude of the oscillations. At sensor position H3, the fluctuation magnitudes is much higher than that in H1 and

H2. This is due to the sensor location. H3 is located at a region of high turbulent impingement on the window.

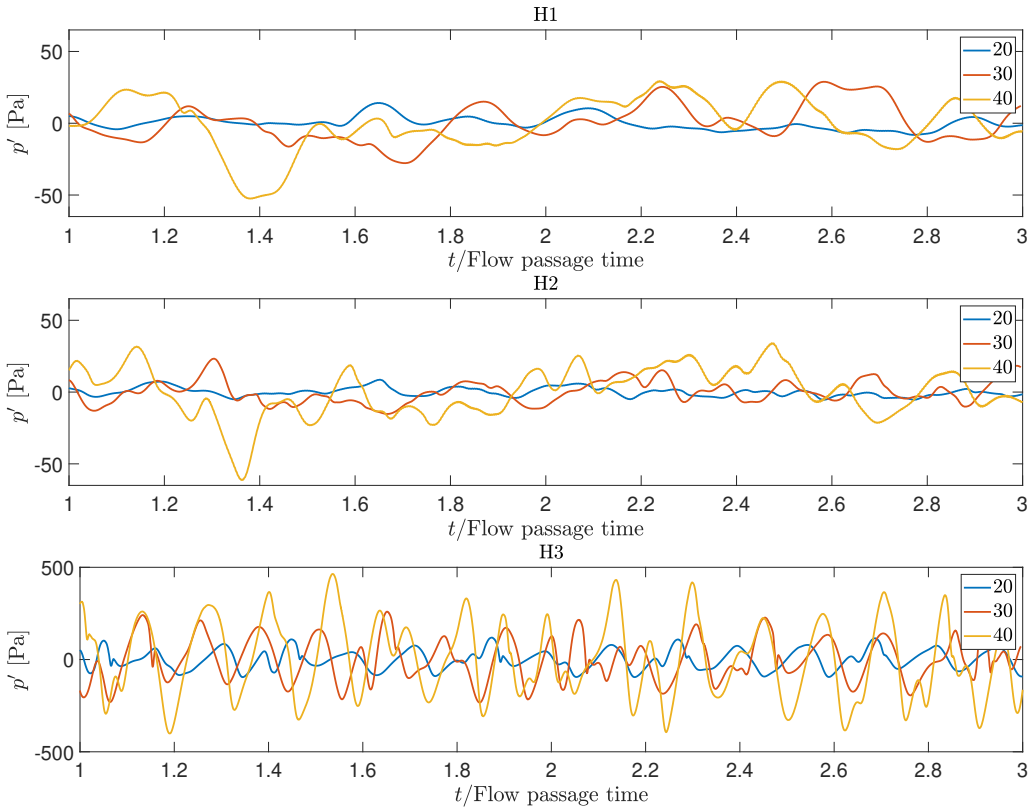

Figure 14: The time history of pressure fluctuations at the sensors H1 (0.1, 0.117, 0.085) m, H2 (0.2, 0, 0) m and H3 (0.498, 0, -0.142) m for the 3 free-stream velocity cases. From top to bottom: H1, H2, H3.

Frequency domain

The data series of every time step for the pressure fluctuations at H1, H2 and H3 are analyzed in the frequency domain. The data is collected after one flow passage time and the total time for analysis is two flow passages time. Figure 15 shows the normalized one-side power spectral density (PSD) of p' at the specified sensors for the three different velocity cases. Table A.2 gives the parameters of the signal-processing approach.

At H1 which is at the back surface of the mirror close to the mirror edge and H2 which is at the plate inside the recirculation region, there are visible peaks around 500 to 1300 Hz. To be specific, the peaks of H1 and H2 are at 570 Hz, 880 Hz and 1230 Hz for 20 m/s, 30 m/s and 40 m/s respectively. It is seen that as the freestream velocity increases, the peak frequency also increases. On the other hand, there is no remarkable peak for H3 at high frequency at any velocity, but it is clearly shown that its signal's power content is overall higher than the other sensors. This is in accordance to the fluctuation amplitudes seen from Figure 14. This phenomenon may suggest that the pressure fluctuations at H3 have a different source from the

other two sensors.

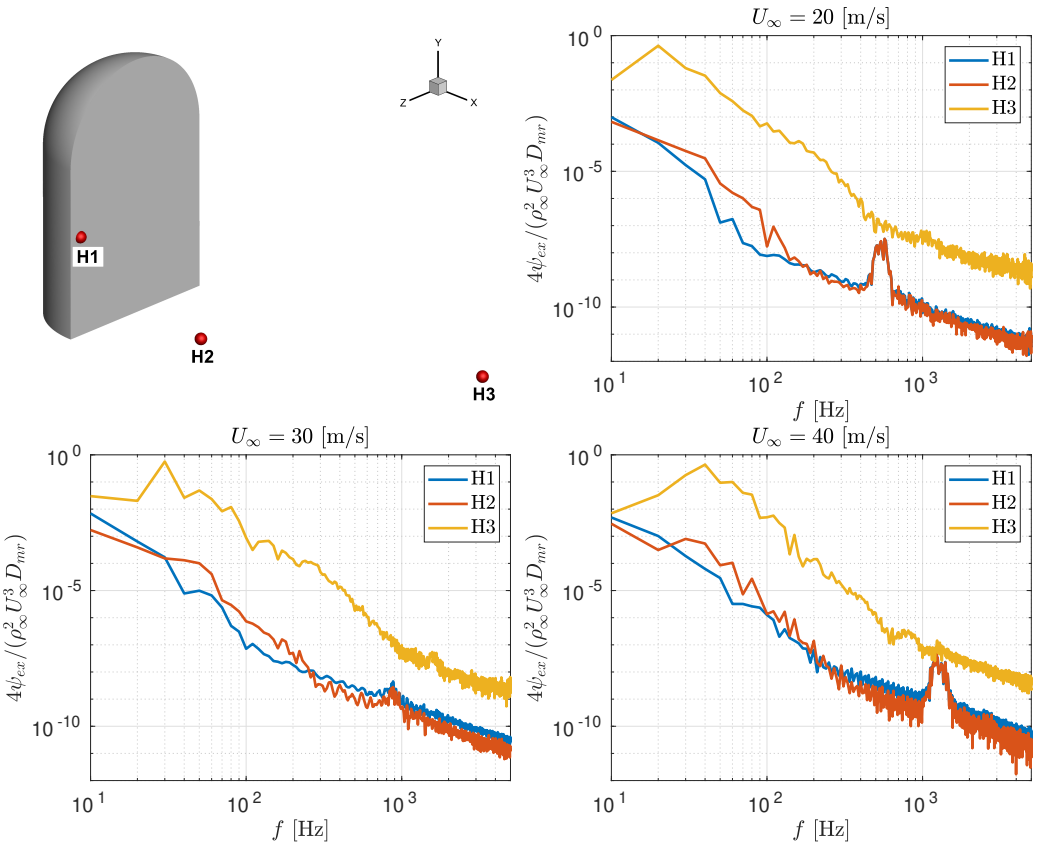

Figure 15: The normalized PSDs of the exterior surface pressure fluctuations at the sensors H1 (0.1, 0.117, 0.085) m, H2 (0.2, 0, 0) m and H3 (0.498, 0, -0.142) m for the 3 free-stream velocity cases

Due to time and computational resource limitations, only the incompressible CFD method has been applied. It should be noted that the incompressible CFD method can only provide the hydrodynamic pressure fluctuation component while in fact, the total pressure fluctuations also include the acoustic component. The hydrodynamic pressure fluctuations here are defined as the pressure fluctuations associated with phenomena like turbulence to be distinguished from acoustic pressure fluctuations which is caused by sound wave propagation. For the noise generated by the generic side mirror, only flow region noise and near field noise needs to be considered, because the far field noise caused by the side mirror is much lower compared to the engine and road-tire noise under same speed and distance [7]. In the flow region, hydrodynamic pressure fluctuations are dominant while in the near field, hydrodynamics and wave propagation are of equal importance. In this project, only hydrodynamic pressure fluctuations have been investigated. But if the acoustic wave equation is introduced, the hydrodynamic pressure fluctuation can be used as a noise source term and the acoustic component can be solved. Figure 15 indicates that there are peaks located at 500-1300 Hz, which means that tonal noise with frequency 500-1300 Hz will be generated and radiated to the surrounding.

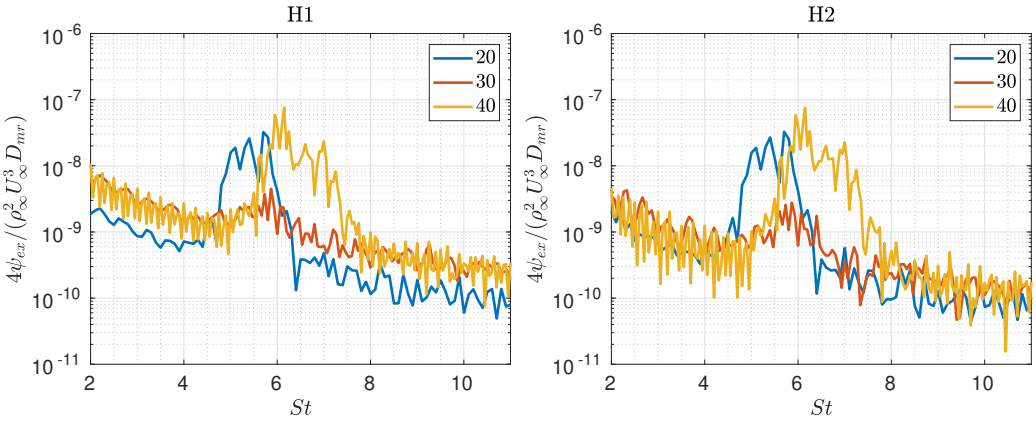

Figure 16: The normalized PSDs of the exterior surface pressure fluctuations at the sensors H1 and H2 versus the Strouhal number. Zoom in view of the PSD peaks

The frequency axis can be normalized for each velocity as the Strouhal number (St) which is fD_{mr}/U_∞. Figure 16 shows the normalized PSD for the peak-containing sensors H1 and H2 as a function of St for each velocity. It can be seen that the power peaks Strouhal number is around 5 to 6 for the three cases. That means those peaks are not due to vortex shedding, whose St is about 0.2 [8], and it can be said that they are caused by coherent structures inside the free shear layer that develops from the edges of the mirror. It should be noted that the pressure fluctuations at H1 and H2 which have a power peak, as seen, generate tonal noise propagation at the same time. On the other hand, less noticeable peaks can be distinguished for H3 at smaller frequencies. Figure 17 reveals that PSD peaks can be seen in H3 for $St = 0.2$. As said, this suggest that the fundamental frequency of this sensor signal is the vortex shedding frequency. Furthermore, H1 and H2 do not exhibit a PSD peak at $St = 0.2$, which implies that pressure fluctuations from H1 and H2 have no common source with H3 pressure fluctuations.

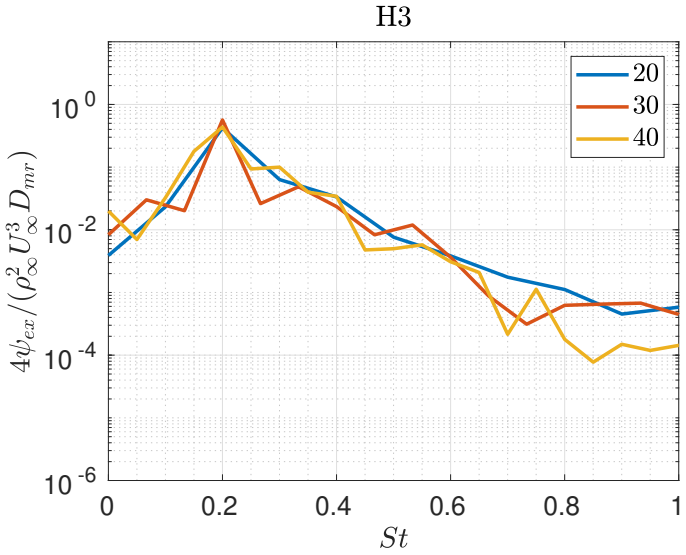

Figure 17: The normalized PSDs of the exterior surface pressure fluctuations at the sensor H3 versus the Strouhal number. Zoom in view of the PSD peak found.

5 Conclusion and future work

In view of how turbulent flow behaves and how pressure fluctuations generate past a generic side-view mirror model, the following considerations can be stated in light of the different simulations and results obtained in the present study.

In the steady field simulation, the different velocity cases (20 m/s, 30 m/s and 40 m/s) have all analogous normalized velocity ($v_x/v_{x,\infty}$) distribution shown in Figure 8. A fast region right on top of the blunt body extending downstream above the recirculation region, as well as a small negative velocity region in bottom-front of the side-view mirror known as the horseshoe vortex can be recognized. The pressure coefficient contour revealed that there is a high pressure region on the front side of the mirror, and as the flow passes through the curved surface and accelerates, a large low pressure area appears in the back of the mirror enclosing the recirculation area. A wall shear stress comparison showed that the recirculation region length is approximately the same for the different velocity cases.

When it comes to the unsteady field simulation, the SST $k-\omega$ model was chosen since it has less damping effect on the fluctuations in the wake region compared with the $k-\varepsilon$ model. The time-averaged pressure coefficients at different sensors show that the URANS simulation, which uses SST $k-\omega$, presents a $\langle C_p \rangle$ that is closer to the experimental data than its steady counterpart where the realizable $k-\varepsilon$ model is used. This confirms that the URANS simulation is a more accurate way of solving the flow, since less modeling is done when every time step is being solved.

From the vorticity snapshots in Figure 13, the vortices originate at the mirror edge becoming unstable as they develop downstream, where they evolve and merge with the larger weak vortices because of viscosity. The creation of these vortices leads to pressure and velocity fluctuations. By comparing the pressure fluctuation magnitudes in Figure 14 for different velocities at the same sensor position, it could distinctly be seen that when the velocity becomes higher, the amplitude of the fluctuations becomes greater. The sensor position H3 is of special interest since it has higher pressure fluctuations magnitude than H1 and H2, hence larger power content. However, the power spectral density analysis shows high peaks at the other sensor locations (H1 and H2) at a Strouhal number $St \approx 6$. These power peaks are caused by coherent structures inside the free shear layer that develop from the mirror edges and they may trigger high frequency tonal noise peaks that propagate as well. On the other hand the main source of pressure fluctuations at H3 is due to vortex shedding phenomena as determined from Figure 17.

As previously discussed, normalized variables of the flow characterization such as velocity v_x and C_p showed that independent of the velocity cases simulated, the flow behaviour within the recirculation region and downstream does not seem to vary considerably. The frequency analysis with the dimensionless Strouhal number also showed that the power peaks are velocity case independent, since these ones are located at the same St positions. Thus it is concluded that, in order to save

computational time and simplify the flow study, the slowest velocity case at 20 m/s can be consider to make the same analysis as for 40 m/s.

An interesting future work is varying the side-view mirror shape and using a more realistic aspect that better resembles the real form of a car's side-view mirror. The present study results can be employed to explore the influence of the different geometries on the flow behaviour and source noise generation.

As described previously, the present study has analyzed only the influence of hydrodynamic pressure fluctuations, since incompressible flow is being assumed. An interesting future research work could either be to drop the incompressible assumption or couple an acoustic wave model, so that the simulation includes the sound waves generation and radiation process that happens in the turbulent boundary layer, and which contributes to the pressure fluctuations sensed on the mirror and window surfaces. The current results, for instance the PSD at the different sensors, can be used to compare the influence that the acoustic waves have on the signal's power.

Since the available experimental data from previous study was obtained more than twenty years ago and only contains pressure coefficients at a series of sensors, it is necessary to carry experiments using more advanced technologies such as particle image velocimetry (PIV) and hot wire anemometer to show more details about the velocity field. Furthermore, the noise level can be measured by setting microphones at interesting positions.

References

[1] David C. Wilcox. *Turbulence modeling for CFD*. DCW Industries, 1994.

[2] F. R. Menter. Two-equation eddy-viscosity turbulence models for engineering applications. *AIAA Journal*, 32(8):1598–1605, 1994. doi: 10.2514/3.12149.

[3] Hua-Dong Yao and Lars Davidson. Vibro-acoustics response of a simplified glass window excited by the turbulent wake of a quarter-spherocylinder body. *The Journal of the Acoustical Society of America*, 145(5):3163–3176, 2019. doi: 10.1121/1.5109548.

[4] R. Höld, A. Brenneis, A. Eberle, V. Schwarz, and R. Siegert. Numerical simulation of aeroacoustic sound generated by generic bodies placed on a plate. i - prediction of aeroacoustic sources. *5th AIAA/CEAS Aeroacoustics Conference and Exhibit*, Oct 1999. doi: 10.2514/6.1999-1896.

[5] R. Siegert, V. Schwarz, and J. Reichenberger. Numerical simulation of aeroacoustic sound generated by generic bodies placed on a plate. ii - prediction of radiated sound pressure. *5th AIAA/CEAS Aeroacoustics Conference and Exhibit*, Oct 1999. doi: 10.2514/6.1999-1895.

[6] Hua-Dong Yao and Lars Davidson. Generation of interior cavity noise due to window vibration excited by turbulent flows past a generic side-view mirror. *Physics of Fluids*, 30(3):036104, 2018. doi: 10.1063/1.5008611.

[7] Jonas Ask. *A Study of Incompressible Flow Fields for Computational Aero Acoustics*. Thesis, Department of Applied Mechanics, 2005.

[8] J. P. Den. Hartog. *Mechanical Vibrations*. Dover Publications, 2013.

A Appendix

Table A.1: Sensor location [m]

S1-S3	(0.094, 0.0666, -0.0998)	(0.094, 0.1334, -0.0998)	(0.094, 0.1666, -0.0998)
S4-S6	(0.094, 0.2, -0.0998)	(0.094, 0.2258, -0.0998)	(0.098, 0.25, -0.0864)
S7-S9	(0.094, 0.286, -0.05)	(0.094, 0.2964, -0.0258)	(0.094, 0.2998, 0.0)
S10-S12	(0.074, 0.2966, 0.0)	(0.05, 0.2866, 0.0)	(0.0292, 0.2708, 0.0)
S13-S15	(0.0134, 0.25, 0.0)	(0.0034, 0.2258, 0.0)	(0.0, 0.2, 0.0)
S16-S18	(0.0, 0.1666, 0.0)	(0.0, 0.1334, 0.0)	(0.0, 0.1, 0.0)
S19-S21	(0.0, 0.0666, 0.0)	(0.0, 0.0334, 0.0)	(0.0034, 0.1334, -0.0258)
S22-S24	(0.0134, 0.1334, -0.05)	(0.0292, 0.1334, -0.0708)	(0.05, 0.1334, -0.0866)
S25-S27	(0.0742, 0.1334, -0.0966)	(0.1, 0.15, 0.085)	(0.1, 0.2842, -0.011)
S28-S30	(0.1, 0.2674, -0.0518)	(0.1, 0.211, -0.0842)	(0.1, 0.15, -0.085)
S31-S33	(0.1, 0.05, -0.085)	(0.1, 0.05, 0.0)	(0.1, 0.2, 0.0)
S34	(0.1, 0.25, 0.0)		

In Table A.2, T denotes the physical time studied and Δf is the frequency resolution for the signal-processing.

Table A.2: The parameters of the signal-processing approach

Case	T (s)	Flow passages	Sampling rate (Hz)	Δf (Hz)
URANS 40	0.4	2	3.33×10^4	10
URANS 30	0.54	2	2.5×10^4	10
URANS 20	0.8	2	1.67×10^4	10